

# Grounded Affordance from Exocentric View

Hongchen Luo, Wei Zhai, Jing Zhang, Yang Cao, and Dacheng Tao, *Fellow, IEEE*

**Abstract**—Affordance grounding aims to locate objects’ “action possibilities” regions, which is an essential step toward embodied intelligence. Due to the diversity of interactive affordance, the uniqueness of different individuals leads to diverse interactions, which makes it difficult to establish an explicit link between object parts and affordance labels. Human has the ability that transforms the various exocentric interactions into invariant egocentric affordance to counter the impact of interactive diversity. To empower an agent with such ability, this paper proposes a task of affordance grounding from exocentric view, *i.e.*, given exocentric human-object interaction and egocentric object images, learning the affordance knowledge of the object and transferring it to the egocentric image using only the affordance label as supervision. However, there is some “interaction bias” between personas, mainly regarding different regions and different views. To this end, we devise a cross-view affordance knowledge transfer framework that extracts affordance-specific features from exocentric interactions and transfers them to the egocentric view. Specifically, the perception of affordance regions is enhanced by preserving affordance co-relations. In addition, an affordance grounding dataset named AGD20K is constructed by collecting and labeling over 20K images from 36 affordance categories. Experimental results demonstrate that our method outperforms the representative models regarding objective metrics and visual quality. Code is released at [github.com/lhc1224/Cross-View-AG](https://github.com/lhc1224/Cross-View-AG).

**Index Terms**—Affordance Grounding, Knowledge Transfer, Benchmark, Exocentric View, Egocentric View

## 1 INTRODUCTION

THE goal of affordance grounding is to locate an object’s region of “action possibilities”. For an intelligent agent, it is necessary to know not only what the object is but also to understand how it can be used [1]. Perceiving and reasoning about possible interactions in local regions of objects is the key to the shift from passive perception systems to embodied intelligence systems that actively interact with and perceive their environment [2, 3, 4]. It has a wide range of applications for robot grasping, scene understanding, action prediction [5, 6, 7, 8, 9, 10].

Affordance is a dynamic property closely related to the interaction between humans and environments [6]. The uniqueness of different individuals leads to diverse interactions, making it difficult to understand how to interact with objects and establish links between object parts and affordance labels [11]. In contrast, humans can easily perceive the object’s affordance region by observing diverse exocentric human-object interactions, and give a unique egocentric definition. As shown in Fig. 1, although different persons hold the racket in different positions due to their habits, the observer can distinguish swingable regions determined by the intrinsic properties (such as the long handle structure) of the racket from a collection of interacting images and transfer the knowledge to the egocentric view, thereby creating a bridge between the object part and the affordance category.

To empower an agent with this ability to perceive the invariant egocentric affordance from various exocentric interactions, this paper first proposes a task of affor-

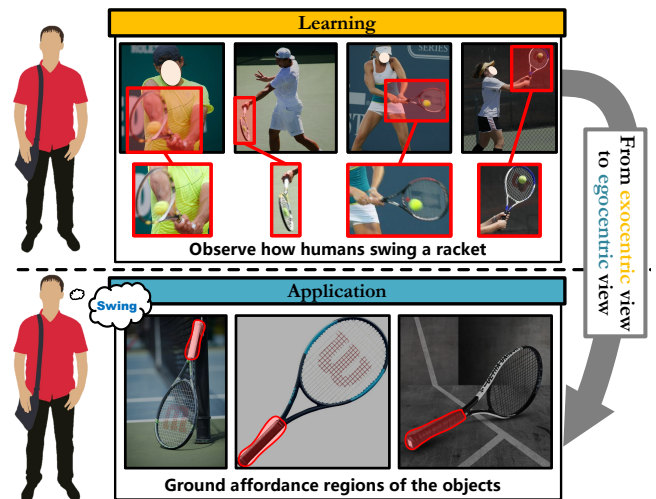


Fig. 1. **Observation.** By observing the exocentric diverse interactions, the human learns affordance knowledge determined by the object’s intrinsic properties and transfers it to the egocentric view.

dance grounding from exocentric view, *i.e.*, given exocentric human-object interactions and egocentric object images, learning affordance knowledge and transferring it to object images by only using affordance labels as supervision. In the testing stage, the output is the prediction of the affordance region for a specific object with the input of an egocentric object image and a particular affordance label.

Bringing this power to real-world scenes would be a major leap forward, but doing so includes an issue with interpersonal “interaction bias” that has both subjective and objective aspects (as shown in Fig. 2). The subjective aspect is due to differences in individual habits leading to diverse interaction regions, making it challenging to locate the affordance region accurately, as shown in Fig 2 (a). However, it is possible to explore the generic features of the affordance regions of objects from multiple human-object interaction

- Hongchen Luo and Wei Zhai have equal contributions.
- H. Luo, W. Zhai and Y. Cao are with University of Science and Technology of China, Y. Cao is also with Institute of Artificial Intelligence, Hefei Comprehensive National Science Center. (E-mail: lhc12, wzhai056@mail.ustc.edu.cn, Forrest@ustc.edu.cn)
- D. Tao is with JD Explore Academy, China and the University of Sydney, Sydney, Australia. (E-mail: dacheng.tao@gmail.com)
- J. Zhang is with the University of Sydney, Sydney, Australia (E-mail: jing.zhang1@sydney.edu.au)

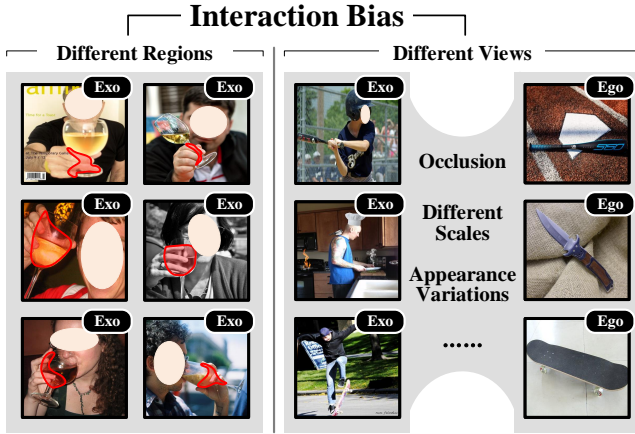


Fig. 2. The main challenge is the “interaction bias” between the personas. (1) “interaction bias” between regions, *i.e.* different habits leading to regional variations in interaction. (2) “interaction bias” between views, due to occlusion, different scales, and apparent variations, the affordance regions of the two views cannot align directly.

images. Thus the diverse interactions can be decomposed into the affordance regions determined by the intrinsic characteristics of objects and the differences in human habits (as shown in Fig. 3 (a)). This paper uses a non-negative matrix factorization [12] to minimize the variation in human habits to obtain affordance features. The objective aspect refers to the occlusion, appearance, and scale differences, making it difficult to directly align the features in the affordance region between views (as shown in Fig. 2 (b)). This paper aligns the affordance regions between the two views by densely matching the affordance-related features extracted from each position of the egocentric feature with those of the exocentric view (as shown in Fig. 3 (b)). Since the subjective factor may affect the accurate representation of the affordance features, resulting in difficulties in accurately aligning under the two views. Hence, this paper first mines the object’s affordance regions from the human-object interaction of multiple images and then aligns the affordance regions under different views by densely matching them. Furthermore, the co-relation between affordance categories is generally existing and independent of object categories (as shown in Fig. 3 (c)). This paper enhances the network’s ability to perceive affordance regions by preserving the co-relation between affordance categories.

In this paper, we propose a **cross-view affordance knowledge transfer framework**. First, an Affordance Invariance Mining (AIM) module is introduced to extract object affordance regions from diverse exocentric interaction regions employing non-negative matrix factorization. Then a Cross-view Feature Transfer module (CFT) is introduced to transfer them to the egocentric view by aligning features. Finally, an Affordance Co-relation Preserving (ACP) strategy enhances the network’s ability to perceive affordance regions by aligning the co-relation of affordance categories from both views. Specifically, the AIM module decomposes the human-object interaction into affordance-related features  $M$  and personal habit differences  $E$ . The non-negative matrix factorization technique minimizes  $E$  to obtain exocentric affordance region features. In the process of alternating iterations, the dictionary bases of the AIM module store the affordance features. The CFT module obtains the match

matrix between the affordance region features from the exocentric view and the object region from the egocentric view through the similarity measure, thereby establishing the mapping relationship of the affordance region between the views, then uses it to transform the affordance features into the egocentric view, and complete the cross-view affordance knowledge transfer by distillation. Finally, the ACP strategy uses cross-entropy loss to align the co-relation matrices of the exocentric and egocentric branches to enhance the network’s ability to perceive and locate affordance regions.

Despite the advances in affordance learning, the existing datasets [13, 14, 15, 16] still bear limitations in terms of affordance/object category, image quality, and scene complexity. To carry out a comprehensive study, this paper presents an affordance grounding dataset named AGD20K, consisting of 20,061 exocentric images and 6,056 egocentric images from 36 affordance categories. We conduct contrastive studies on the AGD20K dataset against nine representative models in four related fields. The results demonstrate our method’s superiority in capturing objects’ intrinsic property and suppressing the interactive diversity of affordance. Our main contributions are summarised as follows:

- 1) We present a affordance grounding from exocentric view task and establish a large-scale AGD20K benchmark to facilitate the research for empowering the agent to capture affordance feature from exocentric interactions.
- 2) We propose a cross-view affordance knowledge transfer framework, in which the affordance knowledge is acquired from exocentric human-object interactions and transferred to egocentric views while preserving the correlation between affordances, thereby achieving better perception and localization of interactive affordance.
- 3) Experiments on the AGD20K dataset demonstrate that our method outperforms representative methods and can serve as a strong baseline for future research.

This paper builds upon our conference version [17], which has been extended in three distinct aspects. **Firstly**, we provide a deeper insight into the problem of interpersonal “interaction bias” in the task caused by different regions and different views. **Secondly**, we introduce a cross-view feature transfer module to effectively align affordance knowledge under the egocentric view by dense comparison. **Thirdly**, we extend the test set from multiple aspects and conduct more experiments on multiple attributes to analyze the model’s performance comprehensively.

The remainder of the paper is organized as follows: Sect. 2 provides a brief overview of existing related work. Sect. 3 describes the proposed pipeline and modules’ details. In Sect. 4, we introduce the collection, annotation, and statistical analysis of the dataset. Sect. 5 describes the experimental setting and provides comprehensive results and analysis. Sect. 6 presents the conclusions, limitations, and potential applications of this work.

## 2 RELATED WORK

### 2.1 Visual Affordance Learning

Visual affordance is a branch of research that considers affordance perception as a computer vision problem based on images or videos, where “action possibilities” regions on

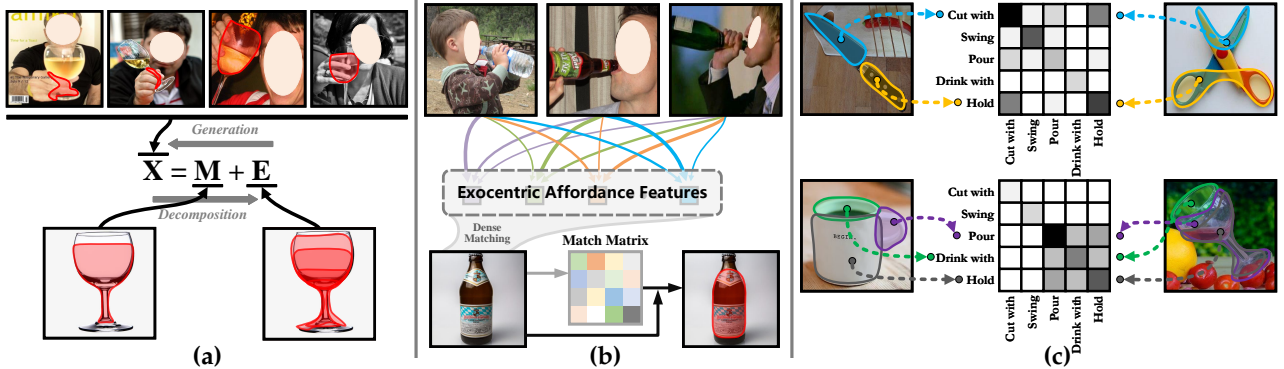


Fig. 3. **Motivation.** (a) Exocentric interactions can be decomposed into affordance-specific features  $M$  and differences in individual habits  $E$  (Sect. 3.1). (b) The model obtains the cross-view match matrix by densely matching the exocentric affordance features with each egocentric location feature and thus obtains the egocentric affordance feature based on the match matrix in an attentive manner (Sect. 3.2). (c) There are co-relations between affordances which are very common due to the multiple affordance properties of objects. This paper enhances the network’s ability to perceive affordance regions by aligning co-relations between views (Sect. 3.3).

objects are detected, segmented, or grounded by machine learning or deep learning methods [18]. Table 1 lists recent works in affordance classification, detection, segmentation, reasoning. A large quantity of previous studies [14, 19, 20, 16, 21, 22] mainly build upon supervised approaches to establish mapping relations between local regions of objects and affordance. Sawatzky *et al.* [23, 24] achieve weakly supervised affordance detection using only a few key points. Deng *et al.* [25] expand affordance detection to 3D scenes. Luo *et al.* [11, 26] explore human purpose-driven object affordance detection in unseen scenarios. Mi *et al.* [27, 28] and Lu *et al.* [29] investigate affordance detection/segmentation in multimodal scenes. Nagarajan *et al.* [3] exploit only affordance labels to ground the interactions from the videos. In contrast to [3], our goal is to empower the agent to learn affordance knowledge from exocentric human-object interactions. To this end, we propose an explicit cross-view affordance knowledge transfer framework that extracts affordance knowledge determined by the intrinsic properties of objects from multiple exocentric interactions and transfers it into egocentric images.

## 2.2 Visual Affordance Dataset

There are a large number of datasets that support affordance-related tasks, as shown in Table 2. Myers *et al.* [15] introduce a large-scale RGB-D dataset containing pixel-level affordance labels and corresponding ranks. Nguyen *et al.* [14] construct the IIT-AFF dataset considering a more complex background of practical applications. Sawatzky *et al.* [23] select video frames to construct a weakly supervised affordance detection dataset, using only cropped-out object regions but in inferior image quality. Luo *et al.* [11] consider inferring human’s purpose from support images and transfers to a group of query images. Then, Lu *et al.* [29] consider multimodal scenarios and extended the PAD to a phase-based affordance detection dataset, but both failed to provide part-level affordance labels. Other datasets [15, 14, 20, 16, 30] face the problems of small scale and low affordance/object category diversity and do not consider human actions to reason about the affordance regions. Chuang *et al.* [20] take the physical world and social norms into account and construct the ADE-Affordance dataset. However, they do not consider the impact of switching to

the exocentric view. In contrast to the above works, we explicitly consider exocentric-to-egocentric view transformations and collect a much larger scale of images, with richer affordance/object classes and part-level annotations, which are more valuable in developing affordance perception approaches towards practical real-world applications.

## 2.3 Learning View Transformations

The existing learning-view transformation works start from the mirror neurons theory [43], which adopt embedding learning to generate perspective invariant representations from paired data, and then leverage it for tasks such as action recognition and video summarization under egocentric view [44, 45, 46, 47, 48, 49]. Sigurdsson *et al.* [44] construct a large-scale video dataset containing first- and third-person pairs, while they use the data to learn joint embeddings in a weakly supervised setting to align the two domains, thus effectively transferring knowledge from third to first person. Fan *et al.* [48] propose to build person-level correspondence across perspectives while introducing a novel semi-Siamese CNN architecture to address this challenge. Li *et al.* [50] extract key egocentric signals from the exocentric view dataset during pre-training and distill them to the backbone to guide feature learning in the egocentric video task. In contrast to the above works, we aim to extract affordance knowledge from the diverse exocentric human-object interactions and transfer it to the egocentric view, which is challenging due to the uncertainty caused by various interactions and the multiple affordance regions that objects contain.

## 3 METHOD

Our goal is to ground the object affordance regions in egocentric images. During training, given a group of exocentric images  $\mathcal{I}_{exo} = \{I_1, \dots, I_N\}$  ( $N$  is the number of exocentric images) and an egocentric image  $I_{ego}$ , the network uses only affordance labels as supervision, to learn affordance knowledge from exocentric images and transfer it to egocentric images. During testing, only given an egocentric image  $I_{ego}$  and the affordance label  $C_a$ , the network outputs the affordance region on the object.

TABLE 1

**Comparison of affordance-related works. Interaction:** the manner in which the drive model discovers affordance. **View:** the viewpoint of the input data. **CV:** cross-view. **SL:** supervised learning. **US:** whether valid on new unseen objects. **Rep:** representation of affordance.

Paper	Interaction	View	CV	SL	US	Rep.	Dataset	Format	Task
[31]	None	Exo	×	Fully	×	Obj	ETHZ Shape [32]	2D	Detection
[33]	Vision	Exo	×	Fully	×	-	NORB [34]	2D	Classification
[22]	Vision	Exo	×	Fully	×	Obj & Tra	CAD-120 [8]	RGBD	Grounding
[35]	Vision	Exo	×	Fully	×	Scene	NYUv2 [36]/UIUC [37]	RGBD	Segmentation
[15], [38], [14], [19], [21], [39]	None	Exo	×	Fully	×	Part	UMD [15], IIT-AFF [14]	RGBD	Segmentation
[40], [23]	None	Exo	×	Weakly	×	Part	[40]	RGBD	Segmentation
[20]	Multimodal	Ego	×	Fully	×	Scene	ADE-AFF [20]	RGB	Segmentation
[16]	Vision	Exo	×	Fully	×	Part	OPRA [16]	RGB	Grounding
[3], [9]	Vision	Exo/Ego	×	Weakly	✓	Part	OPRA [16]/EPIC [41]	RGB	Grounding
[25]	None	Exo	×	Fully	×	Point cloud & Part	3D AffordanceNet [25]	3D	Segmentation
[11]	Vision	Exo	×	Fully	✓	Obj	PAD [11]	RGB	Segmentation
[28], [27]	Language	Exo	×	Fully	×	Obj	[27]	RGB	Detection
[29]	Language	Exo	×	Fully	×	Obj	PAD-L [29]	RGB	Segmentation
[17] & Ours	Vision	Exo/Ego	✓	Weakly	✓	Part	AGD20K	RGB	Grounding

TABLE 2

**Statistics of related datasets and the proposed AGD20K dataset. Part:** part-level annotation. **HQ:** high-quality annotation. **BG:** the background is fixed or from general scenarios. **Exo&Ego:** whether to transfer from exocentric to egocentric view.  $\#Obj$ : number of object classes.  $\#Aff$ : number of affordance classes.  $\#Img$ : number of images.

	Dataset	Pub.	Year	link	HQ	Part	BG	Exo&Ego	$\#Obj$ .	$\#Aff$ .	$\#Img$ .
1	UMD [15]	ICRA	2015	Link	×	✓	Fixed	×	17	7	30,000
2	[23]	CVPR	2017	Link	×	✓	Fixed	×	17	7	3,090
3	IIT-AFF [14]	IROS	2017	Link	×	✓	General	×	10	9	8,835
4	ADE-Aff [20]	CVPR	2018	Link	✓	✓	General	×	150	7	10,000
5	PAD [11]	IJCAI	2021	Link	✓	×	General	×	72	31	4,002
6	PADv2 [26]	IJCV	2022	Link	✓	×	General	×	103	39	30,000
7	AGD20k (Ours)	This Work	2022	Link	✓	✓	General	✓	50	36	26,117

Our proposed cross-view affordance knowledge transfer framework for affordance grounding is shown in Fig. 4. During training, we first use Resnet50 [51] to extract the features of exocentric and egocentric images to obtain  $\mathcal{Z}_{exo} = \{Z_1, \dots, Z_N\}$  and  $Z_{ego}$ , respectively. Then, the Affordance Invariance Mining (AIM) module is introduced to extract affordance-specific clues ( $\mathcal{F}_{exo} = \{F_1, \dots, F_N\}$ ) from the exocentric features (see in Sect. 3.1). Subsequently, the Cross-view Feature Transfer (CFT) module is proposed to transfer the affordance features extracted from the exocentric to the egocentric view (see in Sect. 3.2). Afterward, the features of the two branches ( $\mathcal{F}_{exo}$  and  $F_{ego}$ ) are fed into the same convolution layer to obtain features  $\mathcal{D}_{exo}$  and  $D_{ego}$  respectively. We average the  $\mathcal{D}_{exo}$  through the global average pooling (GAP) layer to obtain the  $d_{exo}$  and pass the  $D_{ego}$  through the GAP layer to get the  $d_{ego}$ . Later,  $d_{exo}$  and  $d_{ego}$  are fed into the same fully connected layer to obtain the affordance prediction. Finally, the Affordance Co-relation Preserving (ACP) strategy is devised to enhance the network’s perception of affordance by aligning the correlation matrix of the outputs of the two views (see in Sect. 3.3). As shown in Fig. 4, during testing, we feed the egocentric object images into the network only through the egocentric branch and then use the CAM [42] technique to obtain the affordance regions of the object (see in Sect. 3.4). Table 3 shows the dimensions, definitions, and meanings of the symbols used in the proposed approach.

### 3.1 Affordance Invariance Mining Module

As shown in Fig. 4, we decompose the interactions in exocentric images into affordance-specific features  $M$  and individual differences  $E$ . Inspired by low-rank matrix fac-

torization [52, 12, 53], we represent the  $M$  as the multiplication of a dictionary matrix  $W$  and a coefficient matrix  $H$ , where the dictionary bases represent the sub-features of human-object interaction and minimize  $E$  by iterative optimization to obtain a reconstructed affordance representation  $M$ . Specifically, for the input  $Z_i$ , we first reduce its dimensionality with a convolution layer and a ReLU layer to ensure the non-negativity of the input and then reshape them into  $X_i \in \mathbb{R}^{c \times h \times w}$  ( $c$ ,  $h$  and  $w$  are the channels, length, and width of the feature maps respectively). We use non-negative matrix factorization [12] to update the dictionary and the coefficient matrices. Consequently,  $X_i$  is decomposed into two non-negative matrices  $W$  and  $H_i$ . Here  $W \in \mathbb{R}^{c \times r}$  is the dictionary matrix shared by all exocentric features, while  $H_i \in \mathbb{R}^{r \times h \times w}$  is the coefficient matrix of each exocentric feature, and  $r$  is the rank of the low-rank matrix  $W$ . To update  $H_i$  and  $W$  in parallel, we concatenate  $\mathcal{X}_{exo} = \{X_1, \dots, X_N\}$  and  $\mathcal{H} = \{H_1, \dots, H_N\}$  to obtain  $X \in \mathbb{R}^{c \times N \times h \times w}$  and  $H \in \mathbb{R}^{r \times N \times h \times w}$ . The optimization process can be formulated as follows:

$$\min_{W, H} \|X - WH\|, \quad s.t. W_{ab} \geq 0, H_{bk} \geq 0. \quad (1)$$

$W$  and  $H$  are updated according to the following rules:

$$H_{ab} \leftarrow H_{ab} \frac{(W^T X)_{ab}}{(W^T W H)_{ab}}, W_{ab} \leftarrow W_{ab} \frac{(X H^T)_{ab}}{(W H H^T)_{ab}}. \quad (2)$$

After several iterations, we get the output  $M = WH$ , and reshape it to  $\mathcal{M}_{exo} = \{M_1, \dots, M_N\}$ ,  $M_i \in \mathbb{R}^{c \times h \times w}$ . Finally, we use a convolution layer to map it to the residual space and sum it with the  $\mathcal{Z}$  to get the final output  $\mathcal{F}_{exo}$ :

$$F_i = \text{ReLU}(Z_i + f(M_i)), \quad i \in [1, N]. \quad (3)$$

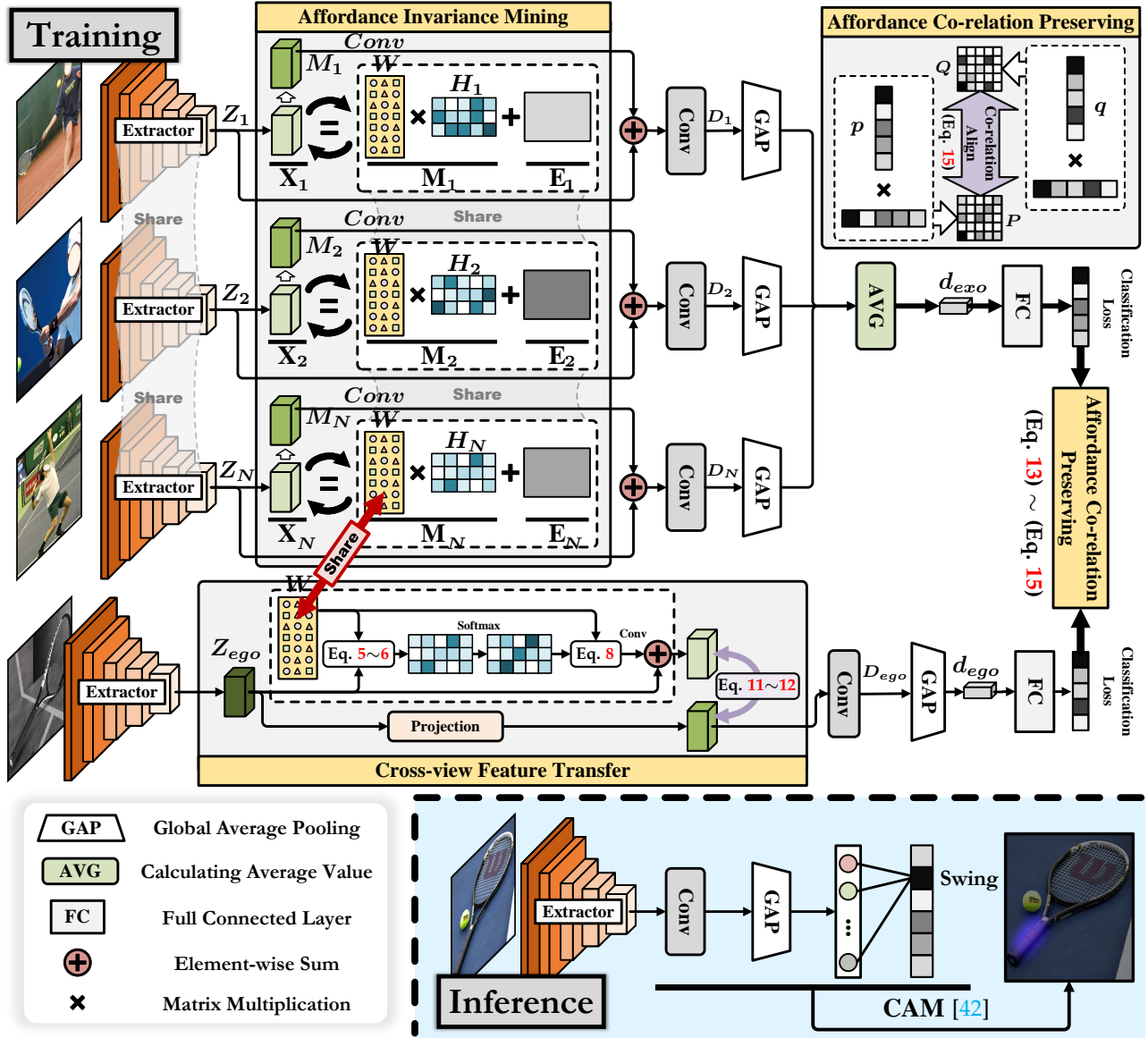


Fig. 4. **Overview of the cross-view affordance knowledge transfer framework.** It mainly consists of an **Affordance Invariance Mining (AIM)** module (Sect. 3.1), a **Cross-view Feature Transfer (CFT)** module (Sect. 3.2) and an **Affordance Co-relation Preserving (ACP)** strategy (Sect. 3.3).

In each batch of training, we update the initial dictionary matrix  $W^{(0)}$  such that it can accumulate the statistical prior of the common subfeature of human-object interaction, *i.e.*,

$$W^{(0)} \leftarrow \alpha W^{(0)} + (1 - \alpha) \bar{W}, \quad (4)$$

where  $\bar{W}$  is the average over each mini-batch.

### 3.2 Cross-view Feature Transfer Module

As shown in Fig. 4, the cross-view feature transfer (CFT) module obtains the cross-view match matrix by densely comparing the similarity between each pixel of the ego-centric feature and the dictionary bases, thus transforming the affordance knowledge into egocentric view, and finally, implementing cross-view knowledge transfer by distillation. Specifically, the egocentric feature is fed through convolution  $f$  and the ReLU layer to align the channels with  $X$  in the AIM module and reshape to  $\mathbb{R}^{c \times h \times w}$  to obtain the feature representation  $Z_{ego}$ . Subsequently, we compute the correlation coefficients of each pixel position in  $Z_{ego}$  with

the bases in the dictionary matrix  $W$  and normalize them by a softmax operation to obtain the match matrix  $H_{ego}$  for  $W$ . Then, the activation feature  $M_{ego}$  is obtained by reconstructing  $W$  and  $H_{ego}$ . Finally,  $M_{ego}$  is reshaped to  $\mathbb{R}^{c \times h \times w}$  and mapped to the same dimension as  $Z_{ego}$  and augmented with the original feature to obtain the activation feature  $\tilde{F}_{ego}$ :

$$X_{ego} = \text{ReLU}(f(Z_{ego})), \quad (5)$$

$$H_{ego} = X_{ego}^T W, \quad (6)$$

$$H_{ego} = \text{Softmax}((H_{ego})), \quad (7)$$

$$M_{ego} = W H_{ego}, \quad (8)$$

$$\tilde{F}_{ego} = \text{ReLU}(f(M_{ego}) + Z_{ego}). \quad (9)$$

Only the egocentric image and the affordance label are input in testing. To enable the egocentric branch to have the ability to perceive the affordance region, we transfer  $\tilde{F}_{ego}$  to the egocentric branch by distillation. First,  $Z_{ego}$  is fed into the project layer  $\text{Project}(\cdot)$  to obtain the feature representation

TABLE 3  
The dimensions, domains of definition, and meanings of the symbols used in the proposed approach.

	Dimensions	Domains	Meanings
$I_i/I_{ego}$	$3 \times 224 \times 224$	$[-1, 1]$	Exocentric/Egocentric image
$Z_i/Z_{ego}$	$2048 \times w \times h$	$[-\infty, +\infty]$	Exocentric/Egocentric feature
$X_i$	$c \times w \times h$	$[0, +\infty]$	$Z_i$ after dimensionality reduction
$X$	$c \times Nhw$	$[0, +\infty]$	$X_i$ reshape after concatenating
$W$	$c \times r$	$[0, +\infty]$	Dictionary matrix
$H$	$r \times Nhw$	$[0, +\infty]$	Coefficient matrix
$M$	$c \times Nwh$	$[0, +\infty]$	Reconstructed from $W$ and $H$
$F_i$	$c \times Nhw$	$[0, +\infty]$	Output of the AIM module
$X_{ego}$	$c \times wh$	$[0, +\infty]$	$Z_{ego}$ after dimensionality reduction
$H_{ego}$	$r \times hw$	$[0, +\infty]$	Coefficient matrix for CFT module
$M_{ego}$	$c \times hw$	$[0, +\infty]$	Reconstructed from $W$ and $H_{ego}$
$\tilde{F}_{ego}$	$c \times h \times w$	$[0, +\infty]$	Activate feature for egocentric
$\hat{F}_{ego}$	$c \times h \times w$	$[0, +\infty]$	Project feature
$D_{exo}$	$1024 \times h \times w$	$[-\infty, +\infty]$	$F_i$ after convolution
$D_{ego}$	$1024 \times h \times w$	$[-\infty, +\infty]$	$F_{ego}$ after convolution
$s/g$	$N_c$	$[-\infty, +\infty]$	Prediction scores
$P/Q$	$N_c \times N_c$	$[0, 1]$	Co-relation matrix

$\tilde{F}_{ego}$ . Then, the maximum response value of each pixel region is selected for alignment. Finally, the knowledge related to affordance is distilled into the egocentric branch by aligning the feature distributions of  $\tilde{V}_{ego}$  ( $\tilde{V}_{ego} \in \mathbb{R}^{h \times w}$ ) and  $\bar{V}_{ego}$  ( $\bar{V}_{ego} \in \mathbb{R}^{h \times w}$ ) through  $L2$  loss:

$$\bar{F}_{ego} = \text{Project}(Z_{ego}), \quad (10)$$

$$\tilde{V}_{ego} = \text{Max}(\tilde{F}_{ego}), \quad \bar{V}_{ego} = \text{Max}(\bar{F}_{ego}), \quad (11)$$

$$L_{KT} = \left\| \tilde{V}_{ego} - \bar{V}_{ego} \right\|, \quad (12)$$

where  $\tilde{V}_{ego}$  and  $\bar{V}_{ego}$  represent the channel maximum response values for each pixel of  $\tilde{F}_{ego}$  and  $\bar{F}_{ego}$ , respectively.

### 3.3 Affordance Co-relation Preserving Strategy

The Affordance Co-relation Preserving (ACP) Strategy is illustrated in Fig. 4. First, we feed the feature representations of the two branches ( $d_{exo}$  and  $d_{ego}$ ) into the same fully connected layer to obtain the prediction scores  $s$  and  $g$ . Then, we align the affordance co-relation between the exocentric and egocentric views by calculating the cross-entropy loss [54]  $L_{ACP}$  of the co-relation matrix of the prediction scores of the two branches:

$$p_j = \frac{\exp(s_j/T)}{\sum_k^{N_c} \exp(s_k/T)}, \quad q_j = \frac{\exp(g_j/T)}{\sum_k^{N_c} \exp(g_k/T)}, \quad (13)$$

$$P = p^T p, Q = q^T q, \quad (14)$$

$$L_{ACP} = - \sum_j^{N_c} \sum_k^{N_c} P_{jk} \log(Q_{jk}), \quad (15)$$

where  $T$  is used to control the degree of attention paid to the correlations between negative labels.  $P_{jk}$  and  $Q_{jk}$  denote the correlation between classes  $j$  and  $k$  in the prediction results. Finally, the total loss can be calculated as:

$$L = \lambda_1 L_{cls} + \lambda_2 L_{ACP} + \lambda_3 L_{KT}, \quad (16)$$

where  $\lambda_1$ ,  $\lambda_2$  and  $\lambda_3$  are hyper-parameters to balance the  $L_{cls}$ ,  $L_{ACP}$  and  $L_{KT}$ .  $L_{cls}$  is the sum of the cross-entropy losses of the classification results of the two branches.

## 3.4 Inference

During the testing process, given only an egocentric image and an affordance label, the network localizes the corresponding affordance region (as shown in Fig. 4). Specifically, we utilize the class activation mapping (CAM) [42] by computing a weighted sum of the feature maps  $D_{ego}^i$  of the last convolutional layer to obtain the affordance region heatmap:  $Y^{C_a} = \sum_i w_i^{C_a} D_{ego}^i$ , where  $C_a$  is the affordance class,  $D_{ego}^i$  is the  $i$ -th layer feature map of  $D_{ego}$ , and  $w_i^{C_a}$  is the weight of the fully connected layer corresponding to the  $i$ -th neuron and the  $C_a$  category.

## 4 DATASET

### 4.1 Dataset Collection

The exocentric images are mainly derived from COCO [55] and HICO [56]. Besides, we also collect from PAD [11], OPRA [16] and UCF101 [57]. We choose images or video frames according to verb/affordance categories. Our goal is to capture affordance cues from diverse individual differences determined by the object’s intrinsic properties rather than imitating individual interactions. Therefore, we select only a portion of the frames interacting with the object for the video dataset. Then, we manually remove images with ambiguous interactions. To enrich the diversity of the dataset, we further collect 2,112 exocentric images according to the affordance category from free-license websites. Meanwhile, according to object categories, we collect 3,755 egocentric images from the Internet with free licenses. All images downloaded from the Internet are downloaded via the [link](#). Some examples are shown in Fig. 5 (a). To analyze the model’s performance on the affordance grounding task more comprehensively from a wide range of different aspects, we expand the AGD20K test set (all images with free licenses are downloaded from the website [Flickr](#)). We select images from a variety of perspectives, such as smaller objects, far from the center, more complex backgrounds, and images containing multiple objects [58, 59] (some examples are shown in Fig. 5 (b)). It makes the new test set more challenging, more suitable for real-world application scenarios, and provides a more comprehensive evaluation of the performance of various models. After the expansion, the AGD20K test set contains 3,034 images and 7,402 heatmaps corresponding to different affordance categories, which can satisfy other research settings such as fully supervised learning. The number of images between the training set, test set, and personas in the AGD20K is shown in Fig. 5 (c).

### 4.2 Dataset Annotation

We select 36 affordance classes commonly used in real-world application scenarios and assign labels to each image based on the interaction between human and object in each exocentric image. Given the object class contained in each affordance class, we assign affordance labels based on the object class in the egocentric images. Fig. 5 (c) shows the confusion matrix between the affordance and the object categories. We adopt heatmaps as part-level labels in the test set to better describe the “action possibilities” (*i.e.*, affordance). Specifically, we refer to the OPRA dataset [16] for annotating interaction regions, and the annotation

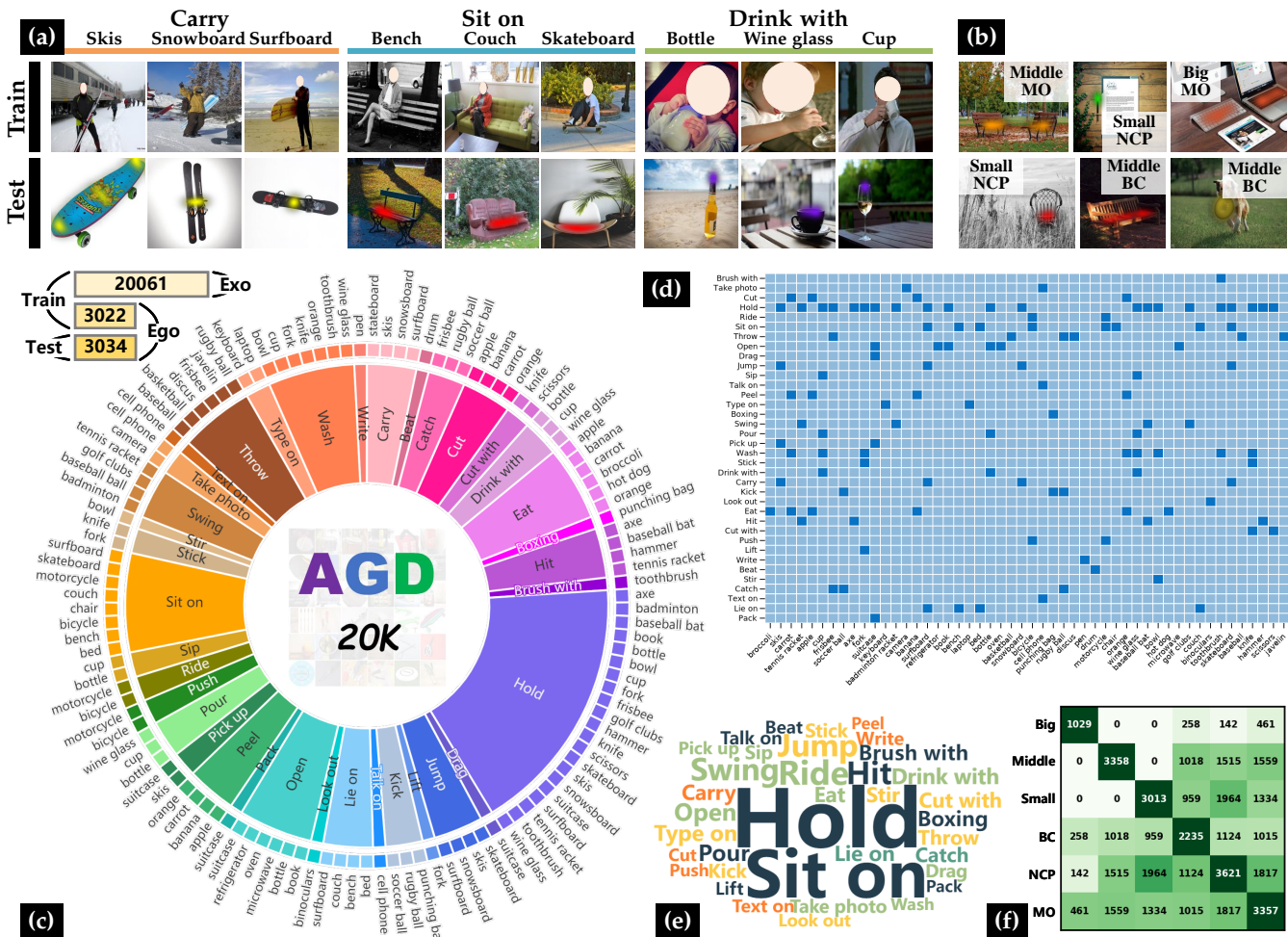


Fig. 5. **Some examples and properties of AGD20K.** (a) Some examples of training and test sets in AGD20K. (b) The distribution of categories in AGD20K. (c) The confusion matrix between the affordance category and the object category in AGD20K, where the horizontal axis denotes the object category, and the vertical axis denotes the affordance category. (d) The word cloud distribution of affordances in AGD20K. (e) The distribution of co-occurring attributes of the AGD20K test set, where “Big”, “Middle”, and “Small” denote images where the area of the mask is more than 0.1, 0.03~0.1, and less than 0.03 of the whole image, respectively. “BC” refers to images with a cluttered background, “NCP” refers to images where the mask is far from the center, and “MO” refers to images with multiple objects in the image.

routine from previous visual saliency works [60, 61, 62]. By observing the interactions between humans and objects in the exocentric images, we label the egocentric images with points of different densities according to the probability of interaction between the human and object regions. In generating the mask, we apply a Gaussian blur to each labeled point and normalize it to obtain the affordance heatmaps. Some examples are shown in Fig. 5 (a).

### 4.3 Statistic Analysis

To obtain deeper insights into our AGD20K dataset, we show its essential features from the following aspects. The distribution of categories in the dataset is shown in Fig. 5 (c), which shows that the dataset contains a wide range of affordance/object categories in diverse scenarios. The confusion matrix of affordance and object categories is shown in Fig. 5 (d). It shows a multi-to-multi relationship between affordance and object categories, posing a significant challenge for the affordance grounding task. Fig. 5 (e) shows the word cloud statistics of AGD20K, implying an unbalanced data distribution, which also satisfies the fact that different interactions occur at different frequencies in the

practice scenario. We divide the test set into three subsets, “Big”, “Middle”, and “Small”, according to the scale of the affordance region, *i.e.*, “Big”: if the proportion of the mask to the whole image is greater than 0.1, “Middle”: if the ratio is between 0.03 and 0.1, and “Small” for the remaining data. Furthermore, we split the test set into three subsets, “BC” (Background Clutter) [63], “NCP” (Negative Central Position) [58] and “MO” (Multiple Objects), according to the image background complexity, distance from the center, and whether it contains multiple objects. Fig. 5 (f) illustrates the confusion matrix for the correlation of different attributes in the test set. Note that one image may have multiple different attributes, which also increases the difficulty of locating affordance regions.

## 5 EXPERIMENTS

### 5.1 Metrics

Previous works mainly segment precise affordance regions [11, 20, 14, 15], while the cross-view affordance grounding task considers a weakly supervised setting that predicts the affordance heatmap using only the affordance category label. Referring to the hotspots grounding-related works

TABLE 4

The results of the different models on the original/additional test set. We compare the results of nine models, Mlnet [64], DeepGazeII [65], EgoGaze , EIL [66], SPA [67], TS-CAM [68], BAS [69], Hotspots [3] and Cross-view-AG [17], on the original test set and the newly added test set. The former represents the results of the original test set and the latter represents the results of the additional test set. The best results are in **bold**.

Method	Seen			Unseen		
	KLD ↓	SIM ↑	NSS ↑	KLD ↓	SIM ↑	NSS ↑
Mlnet [64]	5.197 / 4.506	0.280 / 0.292	0.596 / 0.634	5.012 / 4.567	0.263 / 0.265	0.595 / 0.615
DeepGazeII [65]	1.858 / 1.910	0.280 / 0.265	0.623 / 0.562	1.990 / 2.012	0.256 / 0.238	0.597 / 0.558
EgoGaze [70]	4.185 / 4.362	0.227 / 0.217	0.333 / 0.313	4.285 / 4.612	0.211 / 0.186	0.350 / 0.257
EIL [66]	1.931 / 1.959	0.285 / 0.273	0.522 / 0.577	2.167 / 2.177	0.227 / 0.220	0.330 / 0.286
SPA [67]	5.528 / 5.180	0.221 / 0.249	0.357 / 0.486	7.425 / 7.213	0.169 / 0.186	0.262 / 0.328
TS-CAM [68]	1.842 / 1.897	0.260 / 0.246	0.336 / 0.374	2.104 / 2.015	0.201 / 0.214	0.151 / 0.262
BAS [69]	1.925 / 1.888	0.279 / 0.262	0.702 / 0.701	2.216 / 2.061	0.226 / 0.224	0.531 / 0.548
Hotspots [3]	1.773 / 1.787	0.278 / 0.272	0.615 / 0.701	1.994 / 1.948	0.237 / 0.241	0.577 / 0.626
Cross-view-AG [17]	1.538 / 1.636	0.334 / 0.317	0.927 / 0.939	1.787 / 1.861	<b>0.285</b> / 0.262	0.829 / 0.763
<b>Ours</b>	<b>1.489 / 1.557</b>	<b>0.342 / 0.330</b>	<b>0.981 / 1.026</b>	<b>1.765 / 1.774</b>	<b>0.279 / 0.269</b>	<b>0.882 / 0.907</b>

TABLE 5

The results of different methods on the mixed testset. The best results are in **bold**. “Seen” means that the training set and the test set contain the same object categories, while “Unseen” means that the object categories in the training set and the test set do not overlap. The  $\diamond$  defines the relative improvement of our method over other methods.

Method	Seen			Unseen		
	KLD ↓	SIM ↑	NSS ↑	KLD ↓	SIM ↑	NSS ↑
Mlnet [64]	4.671 $\diamond 67.0\%$	0.289 $\diamond 14.9\%$	0.625 $\diamond 62.6\%$	4.738 $\diamond 62.6\%$	0.264 $\diamond 2.3\%$	0.607 $\diamond 48.4\%$
DeepGazeII [65]	1.899 $\diamond 19.0\%$	0.268 $\diamond 23.9\%$	0.576 $\diamond 76.4\%$	2.007 $\diamond 11.8\%$	0.242 $\diamond 11.6\%$	0.567 $\diamond 58.9\%$
EgoGaze [70]	4.322 $\diamond 64.4\%$	0.219 $\diamond 51.6\%$	0.318 $\diamond 219.5\%$	4.538 $\diamond 61.0\%$	0.192 $\diamond 40.6\%$	0.278 $\diamond 224.1\%$
EIL [66]	1.953 $\diamond 21.1\%$	0.276 $\diamond 20.3\%$	0.564 $\diamond 80.1\%$	2.175 $\diamond 18.6\%$	0.222 $\diamond 21.6\%$	0.296 $\diamond 204.4\%$
SPA [67]	5.259 $\diamond 70.7\%$	0.243 $\diamond 36.6\%$	0.456 $\diamond 122.8\%$	7.261 $\diamond 75.6\%$	0.182 $\diamond 48.4\%$	0.310 $\diamond 190.6\%$
TS-CAM [68]	1.884 $\diamond 18.3\%$	0.249 $\diamond 33.3\%$	0.365 $\diamond 178.4\%$	2.112 $\diamond 16.1\%$	0.198 $\diamond 36.4\%$	0.078 $\diamond 1055.1\%$
BAS [69]	1.897 $\diamond 18.8\%$	0.267 $\diamond 24.3\%$	0.702 $\diamond 44.7\%$	2.096 $\diamond 15.5\%$	0.225 $\diamond 20.0\%$	0.534 $\diamond 68.7\%$
Hotspots [3]	1.788 $\diamond 13.9\%$	0.273 $\diamond 21.6\%$	0.679 $\diamond 49.6\%$	1.959 $\diamond 9.6\%$	0.240 $\diamond 12.5\%$	0.615 $\diamond 46.5\%$
Cross-view-AG [17]	1.613 $\diamond 4.5\%$	0.321 $\diamond 3.5\%$	0.936 $\diamond 8.5\%$	1.845 $\diamond 4.0\%$	0.267 $\diamond 1.3\%$	0.778 $\diamond 15.8\%$
<b>Ours</b>	<b>1.540</b> $\pm 0.003$	<b>0.332</b> $\pm 0.001$	<b>1.016</b> $\pm 0.012$	<b>1.771</b> $\pm 0.013$	<b>0.270</b> $\pm 0.002$	<b>0.901</b> $\pm 0.024$

TABLE 6  
Parameters (M) and inference time (s) for all models.

Method	Mlnet [64]	DeepGazeII [65]	EgoGaze [70]	EIL [66]	SPA [67]	TS-CAM [68]	BAS [69]	Hotspots [3]	Cross-view-AG [17]	Ours
Param. (M)	15.45	20.44	46.53	42.41	69.28	85.86	53.87	132.64	120.03	82.27
Time (s)	0.006	3.760	0.026	0.019	0.081	0.023	0.057	0.087	0.023	0.022

[16, 3, 71], we adopt heatmaps to give a better description of the “action possibilities” (i.e., affordance) and use KLD [61], SIM [63], and NSS [72] to evaluate the probability distribution correlation between the predicted affordance heatmap and Ground Truth (GT).

- Kullback-Leibler Divergence (KLD) [61] measures the distribution difference between the prediction ( $P$ ) and the ground truth ( $Q$ ). It is computed as follows:

$$KLD(P, Q^D) = \sum_i Q_i^D \log \left( \epsilon + \frac{Q_i^D}{\epsilon + P_i} \right), \quad (17)$$

where  $\epsilon$  is a regularization constant.

- Similarity (SIM) [63] measures the similarity between the prediction map ( $P$ ) and the continuous ground truth map ( $Q^D$ ). It is computed as follows:

$$SIM(P, Q^D) = \sum_i \min(P_i, Q_i^D), \quad (18)$$

where  $\sum_i P_i = \sum_i Q_i^D = 1$ .

- Normalized Scanpath Saliency (NSS) [72] measures the correspondence between the prediction map ( $P$ ) and the ground truth ( $Q^D$ ). It is computed as follows:

$$NSS(P, Q^D) = \frac{1}{N} \sum_i \hat{P} \times Q_i^D, \quad (19)$$

where  $N = \sum_i Q_i^D$ ,  $\hat{P} = \frac{P - \mu(P)}{\sigma(P)}$ .  $\mu(P)$  and  $\sigma(P)$  are the mean and standard deviation of  $P$ , respectively.

## 5.2 Comparison Methods

We choose nine advanced methods in four relevant fields such as saliency detection (Mlnet [64], DeepGazeII [65], EgoGaze [70]), weakly supervised object localization (EIL [66], SPA [67], TS-CAM [68], BAS [69]), affordance grounding (Hotspots [3]) and Cross-view affordance knowledge transfer (Cross-view-AG [17]) for comparison.

- **Mlnet [64]**: The model fuses feature extracted from different CNN layers. It contains three main blocks: feature extraction CNN, feature encoding network (weighting of low and high features), and a prior learning network.
- **DeepGazeII [65]**: Unlike other saliency models, it does not perform additional fine-tuning of the VGG features and only trains some output layers to predict saliency on top of VGG [73].
- **EgoGaze [70]**: It is a hybrid gaze prediction model that integrates task-dependent attention transition with bottom-up saliency prediction.

For saliency detection models, we use models trained on the saliency datasets and test in the same way as [3].

- **EIL [66]**: It introduces a novel adversarial erasing technique jointly exploring highly response class-specific

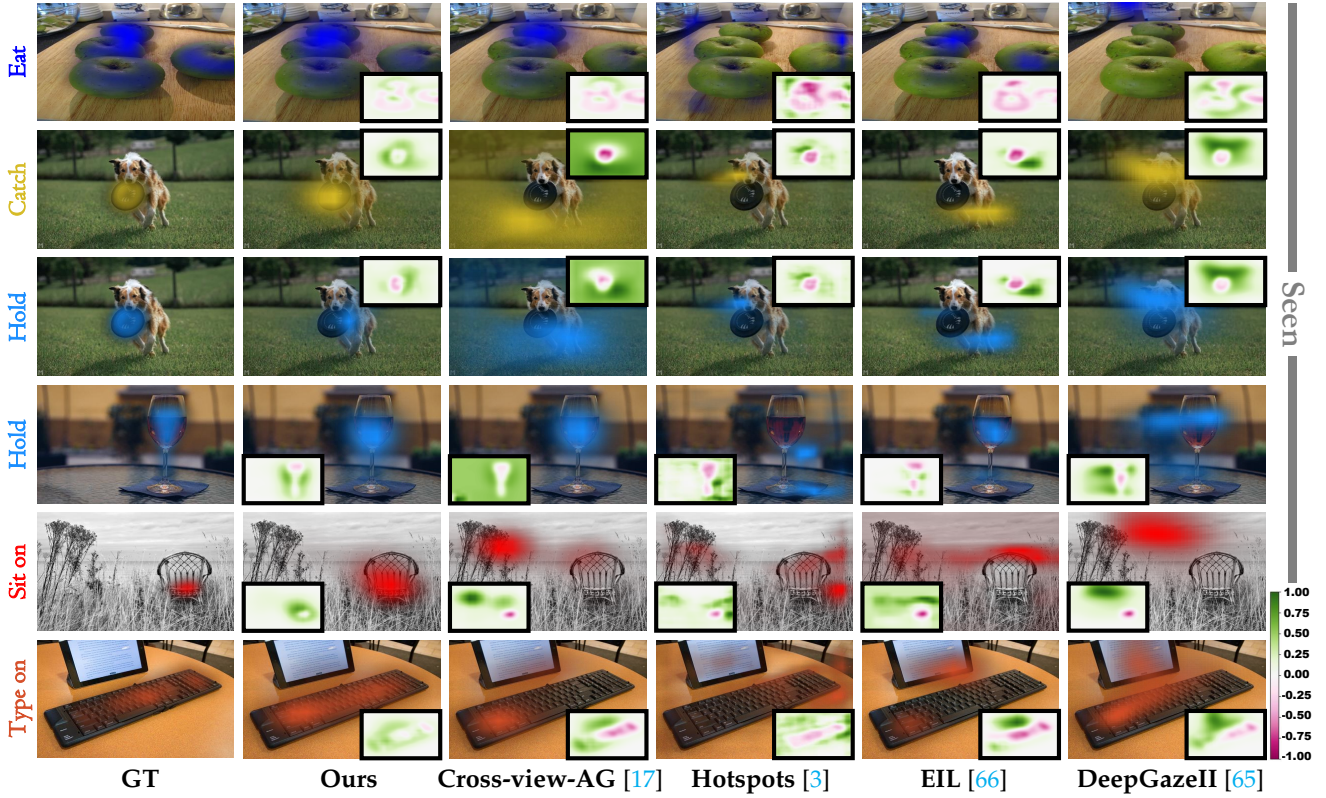


Fig. 6. **Visual affordance heatmaps difference maps at the “Seen” setting.** We select results from representative models, such as cross-view affordance knowledge transfer (Cross-view-AG [17]), affordance grounding (Hotspots [3]), weakly supervised object localization (EIL [66]) and saliency detection (DeepGazeII [65]) for presentation. The difference maps represent the difference between the prediction and the GT.

areas and less discriminative regions to obtain a complete object region.

- **SPA [67]:** It explores how to extract object structure information during training and proposes a structure-preserving activation method that leverages the structure information incorporated in the convolutional features for WSOL.
- **TS-CAM [68]:** It proposes a token semantic coupled attention map to take full advantage of the self-attention mechanism in visual transformer for long-range dependency extraction.
- **BAS [69]:** The model promotes the foreground map generation by introducing an activation mapping constraint module that mainly facilitates the learning of predicted maps by suppressing background activation, leading to more fine-grained prediction results.

For the weakly supervised object localization models, we only utilize exocentric images for training.

- **Hotspots [3]:** It is a weakly supervised way to learn the affordance of an object through video, and affordance grounding is achieved only through action labels.
- **Cross-view-AG [17]:** The model extracts affordance invariance cues from diverse exocentric interactions and transfer it to egocentric view. Besides, by preserving the affordance co-relation, it enhances the perception of the affordance regions.

### 5.3 Implementation Details

Our model is implemented in PyTorch and trained with the SGD optimizer. With random horizontal flipping, the input

images are randomly cropped from  $256 \times 256$  to  $224 \times 224$ . We train the model for 35 epochs on a single NVIDIA 3090ti GPU with an initial learning rate of  $1e-3$ . The hyper-parameters  $\lambda_1$ ,  $\lambda_2$  and  $\lambda_3$  are set to 1, 0.5 and 0.5, respectively. We set the batch size to 32, and the number of exocentric images  $N$  is set to 3. The hyper-parameter  $T$  in the ACP strategy is set to 1. The dictionary matrix  $W$ 's rank  $r$  and the number of iterations in the AIM module are set to 64 and 6, respectively. The number of channels of input features in the AIM module is 64. We divide the dataset into “Seen” and “Unseen”, in which “Seen” means that the training and test sets contain the same class of objects, while “Unseen” indicates that the training and test sets contain different classes of objects. The “Unseen” split can be used to further evaluate the generalization ability of the models. For the other methods, we use Resnet50 [51] as the backbone and the same data augmentation method and batch size. For weakly supervised object localization models (EIL [66], SPA [67], TS-CAM [68] and BAS [69]), the input is exocentric images during training, while the test input is egocentric images. For Hotspots [3], three images are randomly sampled from the exocentric images during training and used as input to the video branch.

### 5.4 Quantitative and Qualitative Comparisons

We first test the performance of the different models on the original test set and the newly supplemented test set (as shown in Table 4). The scores before the slash are the results on the original test set, while the scores after the slash are the results on the newly established test set. For

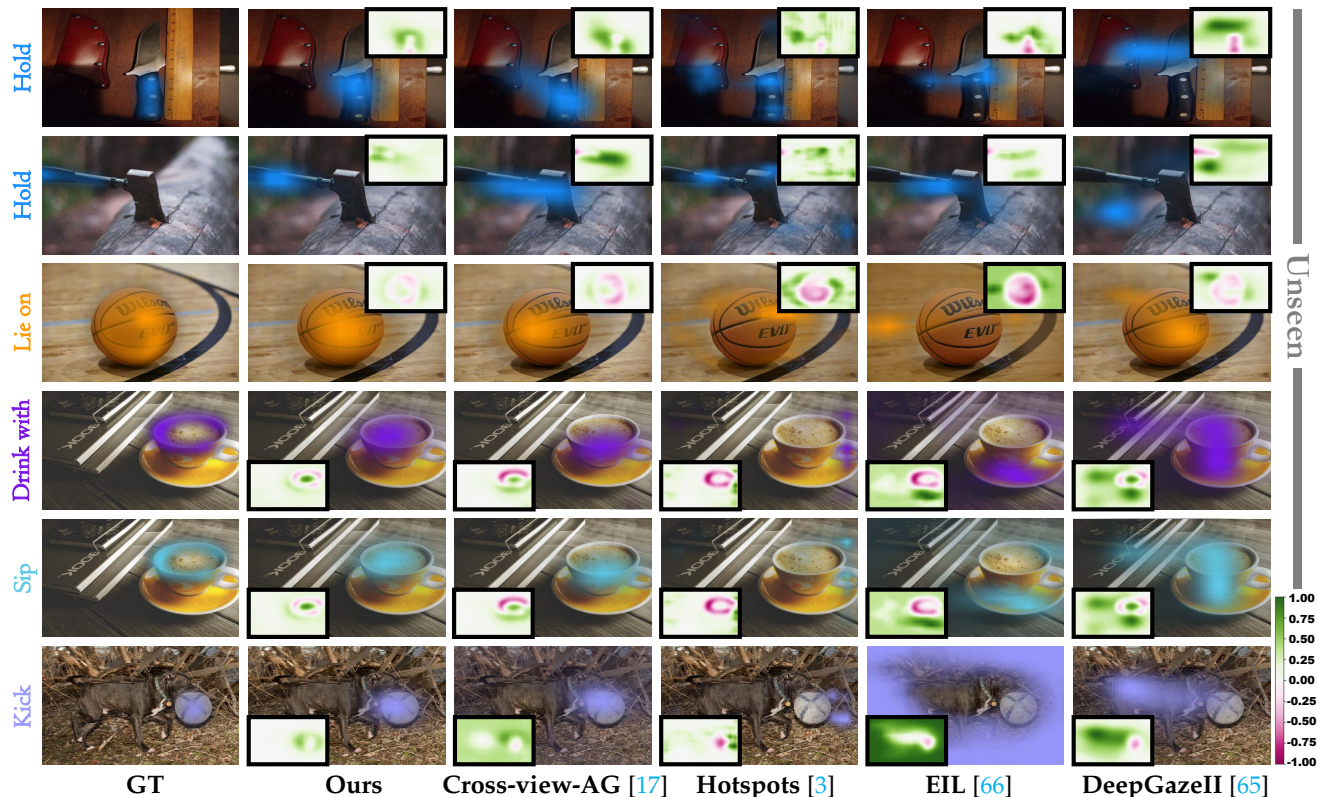


Fig. 7. **Visual affordance heatmaps and difference maps at the “Unseen” setting.** We select results from representative models, such as cross-view affordance knowledge transfer (Cross-view-AG [17]), affordance grounding (Hotspots [3]), weakly supervised object localization (EIL [66]) and saliency detection (DeepGazeII [65]) for presentation. The difference maps represent the difference between the prediction and the GT.

TABLE 7

**Long Tail Distribution.** We divide AGD20K into two subsets (“Head” and “Tail”, according to the number of images in the affordance class), and test the performance of the models in the two subsets separately.

Method						
	Head			Tail		
	KLD ↓	SIM ↑	NSS ↑	KLD ↓	SIM ↑	NSS ↑
Mlnet [64]	4.968	0.274	0.624	4.138	0.310	0.626
DeepGazeII [65]	1.936	0.251	0.571	1.886	0.266	0.520
EgoGaze [70]	4.345	0.219	0.354	4.385	0.215	0.238
EIL [66]	2.016	0.269	0.571	2.039	0.270	0.371
SPA [67]	3.689	0.239	0.436	7.322	0.239	0.360
TS-CAM [68]	1.748	0.265	0.660	2.052	0.226	0.018
BAS [69]	2.117	0.237	0.569	1.887	0.266	0.520
Hotspots [3]	1.829	0.261	0.644	1.830	0.275	0.558
Cross-view-AG [17]	1.656	0.297	0.893	1.670	0.326	0.785
<b>Ours</b>	<b>1.585</b>	<b>0.309</b>	<b>0.975</b>	<b>1.616</b>	<b>0.336</b>	<b>0.858</b>

models such as DeepGazeII [65], EIL [66], and Cross-view-AG [17], which perform better in the original test set, they all show a performance drop on the new test set. BAS [69] obtains more accurate segmentation results by suppressing background regions. Thus there is no particular impact on performance for attributes such as complex backgrounds. However, it is not easy to obtain accurate part-level localization. Compared to the previous state-of-the-art Cross-view-AG [17] approach, the performance of our model degrades less on the new test set. Moreover, the evidence is more obvious on the “Unseen” setting, demonstrating the better

TABLE 8

**Different sources.** “Exo” means simply using exocentric images, while “Both” means using both exocentric and egocentric images in training.

Method	Source	Seen			Unseen		
		KLD ↓	SIM ↑	NSS ↑	KLD ↓	SIM ↑	NSS ↑
EIL [66]	Exo	1.953	0.276	0.564	2.175	0.222	0.296
	Both	2.037	0.304	0.727	6.519	0.214	0.464
SPA [67]	Exo	5.259	0.243	0.456	7.261	0.182	0.310
	Both	4.481	0.262	0.528	6.519	0.214	0.464
TS-CAM [68]	Exo	1.884	0.249	0.365	2.112	0.198	0.078
	Both	1.819	0.266	0.522	2.013	0.217	0.271
BAS [69]	Exo	1.897	0.267	0.702	2.096	0.225	0.534
	Both	2.103	0.282	0.692	1.868	0.238	0.841
<b>Ours</b>	<b>Both</b>	<b>1.540</b>	<b>0.332</b>	<b>1.016</b>	<b>1.771</b>	<b>0.270</b>	<b>0.901</b>

robustness of our model in complex scenarios.

The subsequent experiments and the corresponding analyses are conducted on a combined dataset consisting of a mixture of the original and the new tested sets. Table 5 shows the results for different related models, and it is evident that our approach achieves the best results for all metrics on both the Seen and Unseen settings. Taking KLD as the metric, our method improves **18.9%** compared to the best saliency model, **18.3%** over the best weakly supervised object localization (WSOL) model, **13.9%** over the affordance grounding model, and **4.5%** over the best cross-view affordance knowledge transfer model in the “Seen” setting. Our method on the “Unseen” setting improves **11.8%** compared to the best saliency model, surpasses the best WSOL model by **15.5%**, exceeds the affordance grounding model by **9.6%**, and outperforms the cross-view affordance knowledge transfer model by **3.7%**. Fig. 6 and Fig. 7 show

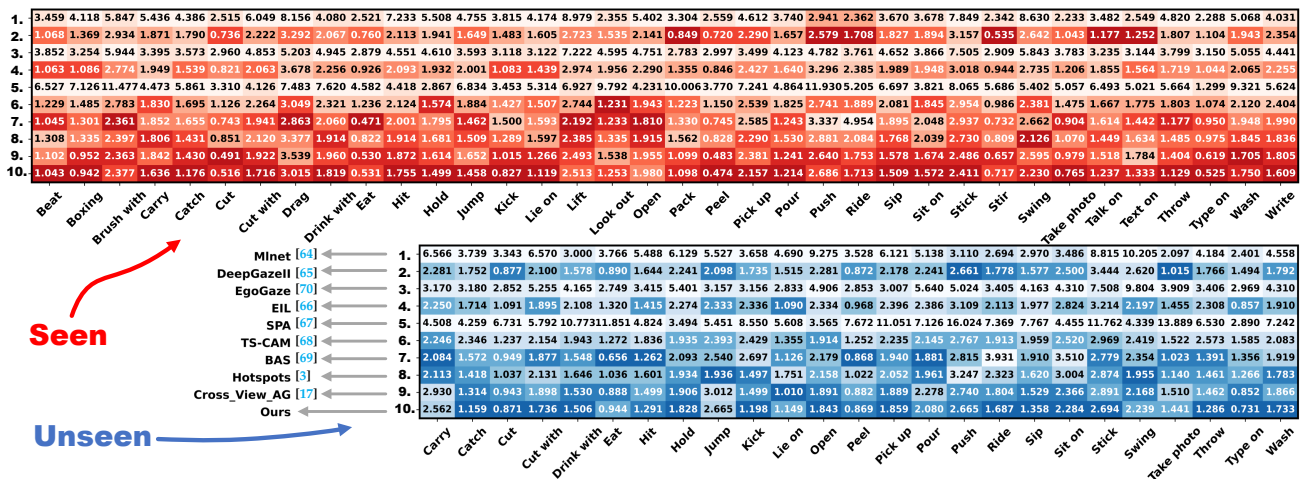


Fig. 8. The results of the different methods on the AGD20K for each affordance category. We calculate the KLD metrics for each affordance category in both “Seen” and “Unseen” settings, with darker colors representing better model performance.

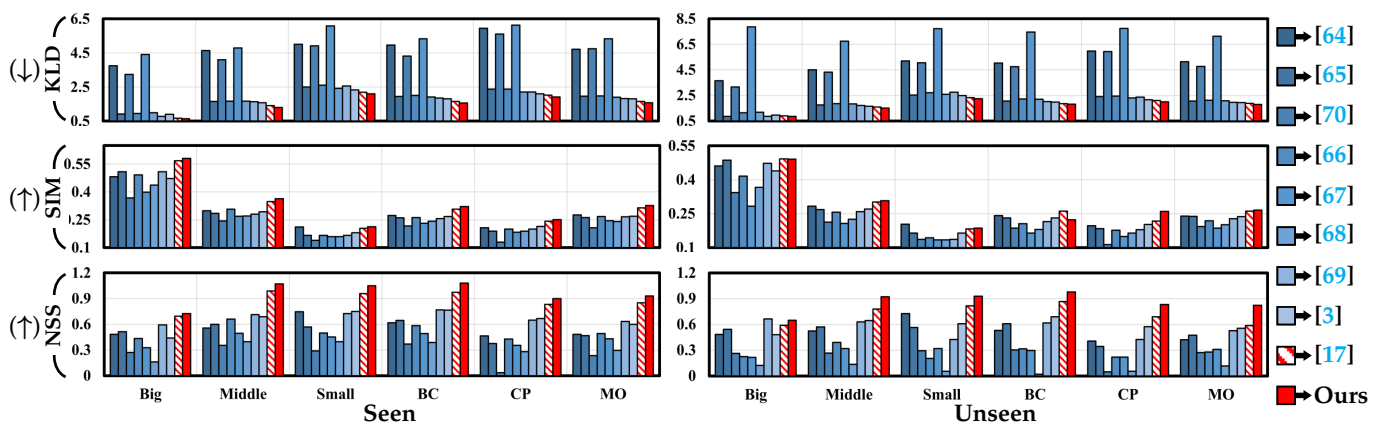


Fig. 9. The results of the models test with different attributes. We divide the test set into six subsets according to the attributes described in Sect. 4.3 and test the performance of different models in each of these subsets. The left side shows the results of the experiment in the “Seen” setting and the right side shows the results in the “Unseen” setting.

the affordance maps in the “Seen” and “Unseen” settings and the difference maps between the predicted results and the ground truth. Compared to other models, our method can more accurately locate the affordance region of the object. Specifically, the red areas in the difference map are generally small and light, which indicates that our method can generate a more complete affordance region of the object. Our model can localize multiple affordance regions for scenes containing multiple objects (e.g., the first row of Fig. 6). For images with complex backgrounds (e.g., Fig. 6, row 5 and Fig. 7, row 6), the model also can locate the affordance regions more accurately, indicating that our method is still robust in complex scenes. For the cases where an object belongs to more than one affordance class or the same affordance contains multiple object classes with vastly different appearances, the model can accurately find the corresponding region, demonstrating that our method can effectively address the challenges posed by multiple possibilities of affordances.

## 5.5 Performance Analysis

**Long Tail Distribution.** The AGD20K dataset has a long-tailed distribution with highly unbalanced data (as shown in Table 7). Thus, we select “Head” and “Tail” classes and test them separately. The results are shown in Table

TABLE 9  
**Ablation study.** We investigate the influence of the AIM module, CFT module and ACP strategy on model performance.

AIM	CFT	ACP	Seen			Unseen		
			KLD ↓	SIM ↑	NSS ↑	KLD ↓	SIM ↑	NSS ↑
✓			1.780	0.304	0.779	2.010	0.242	0.568
	✓		1.735	0.311	0.823	1.977	0.248	0.598
		✓	1.755	0.315	0.809	1.946	0.257	0.683
✓	✓		1.633	0.321	0.922	1.887	0.261	0.729
✓		✓	1.650	0.306	0.929	1.916	0.255	0.695
✓	✓	✓	1.540	0.332	1.016	1.771	0.270	0.901

7. Our model outperforms the other methods in both the “Head” and “Tail” subsets, which is probably due to the ACP strategy that preserves the association between affordance classes and enhances the network’s ability to perceive classes with only small amounts of data.

**Different Sources.** To validate that the superiority of our method is not due to the additional egocentric images, we retrained the weakly supervised object localization models using both exocentric and egocentric images as input. The results are shown in Table 8. It shows that using both exocentric and egocentric images improves most methods. However, the improvement is limited, and more samples cannot provide significant gains. Our method still surpasses all models, showing that explicit knowledge transfer can

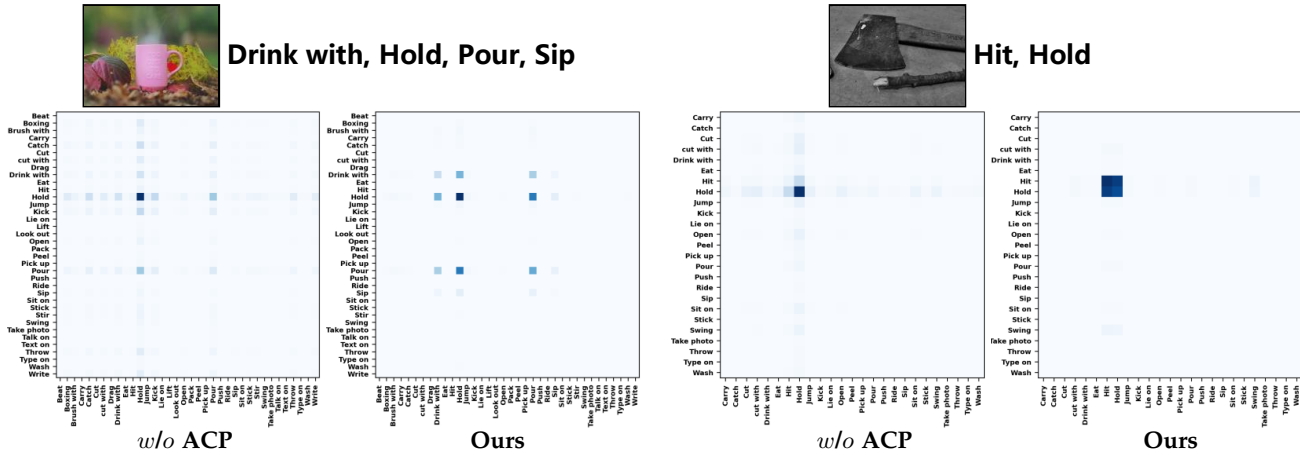


Fig. 10. Visualization of the co-relation matrix. We visualize the co-relation matrix of the models with or without the ACP strategy.

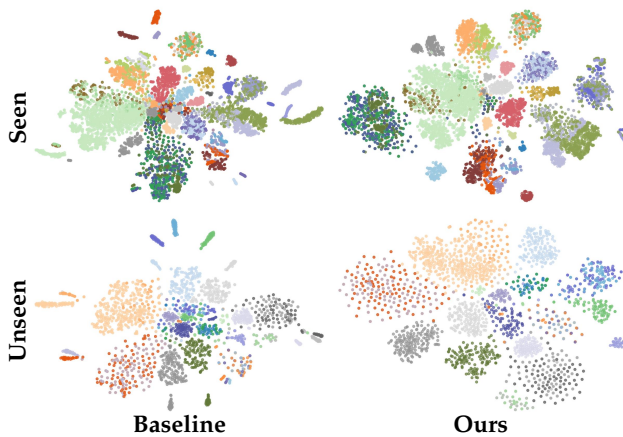


Fig. 11. T-SNE visualization results. The T-SNE results for the baseline without any modules and our model. The first row is the “Seen” setting and the second row is the “Unseen” setting. Due to the small number of images in the “Unseen” setting, the results in the second row are sparse.

effectively transfer affordance knowledge to egocentric and obtain more accurate localization results.

**Different Classes.** Fig. 8 shows the results of the KLD metrics for each category in both “Seen” and “Unseen” settings, with deeper colors indicating better performance. Our model achieves the best results under most affordance categories, demonstrating our method’s superiority in locating affordance regions. In the “Seen” setting, our model obtains more accurate results for both the affordance categories “Hold” and “Cut with”, where there are some co-relations, demonstrating that our approach can enhance the network’s perception of affordance regions by aligning the co-relation of the two views. For affordance categories such as “Pour” and “Carry”, where the interaction habits of different humans are quite diverse, our method still exceeds all other models, validating the effectiveness of the AIM module in extracting affordance-specific features for localization. In the “Unseen” setting, our model achieves promising results for the categories “Pick up”, “Sit on”, *etc.*, with large variations between the object appearances in the training and test sets, demonstrating that our method has a strong generalization capability to new object categories.

**Different Attributes.** Fig. 9 shows the results for all models on different attributes (Big, Middle, Small, BC, NCP, and

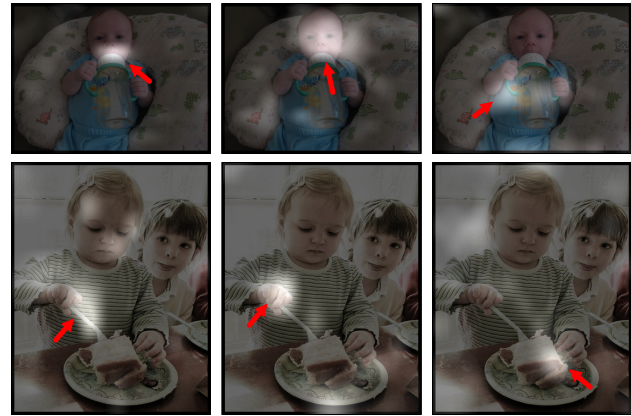


Fig. 12. Visualization of the coefficient matrix  $H$  for the last iteration of the AIM module. We choose maps activated by different bases.



Fig. 13. Visualization of the CFT module output features.

MO). Our approach outperforms other models in almost all settings. In the challenging “Small” subset, our method still produces relatively strong results in terms of both KLD and NSS metrics. Although the results are decreasing in the SIM metric, they still outperform the other methods. In the three subsets of “BC”, “MO”, and “NCP”, our model achieves superior results to the other models, indicating that our method is more robust and can accurately locate the affordance regions of the object.

## 5.6 Ablation Study

To investigate the impact of the AIM module, the CFT module, and the ACP strategy, we evaluate all combinations of them, as shown in Table 9. Note that since the matching of affordance regions in the CFT module requires an optimized dictionary base matrix in the AIM module, the presence of the CFT module must be dependent on the AIM module.

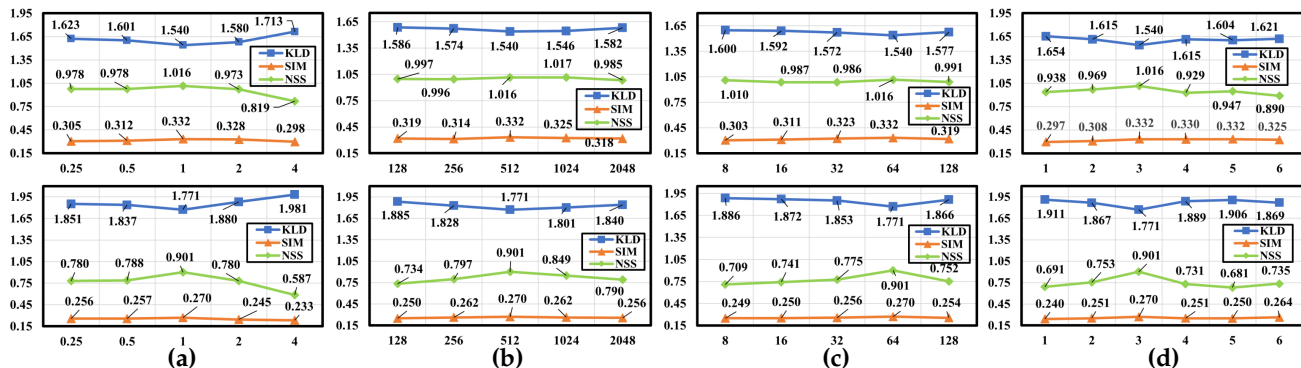


Fig. 14. **Different Hyper-parameters.** We explore (a) the effects of different  $T$  values in the ACP strategy, (b) different number of channels  $c$  in the input features in the AIM module, (c) different rank  $r$  of the dictionary matrix in the AIM module, and (d) different number of exocentric images  $N$  on the model performance. The first and second rows show the results of the experiments with the “Seen” and “Unseen” settings respectively.



Fig. 15. **Failure cases.** Some examples of the model’s failure in slender structures, complex structures and indistinct front and back views.

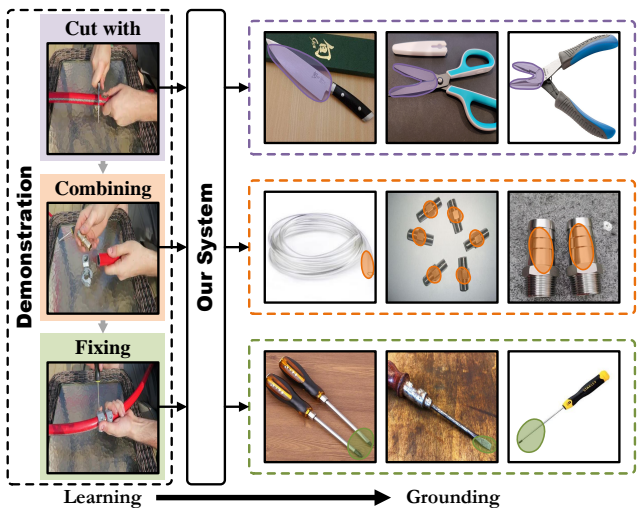


Fig. 16. **Potential Applications: Learning from demonstrations.** Our system can quickly extract the interaction region from the human demonstration image and locate it in the egocentric image.

It indicates that the AIM module extracts invariant affordance features from the diverse interactions of exocentric views, which enables the model to extract affordance-related features quickly. Meanwhile, the ACP strategy can enhance the perception of the affordance region by aligning the correlation of the two branches. We make the T-SNE feature visualization of our model and baseline, as shown in Fig. 11. It shows that our method has more explicit discriminative boundaries and can distinguish different affordance features more accurately. Fig. 12 shows the visualization of the coefficient matrix  $H$  in the AIM module, where we choose maps activated by different bases. It indicates that different bases in the AIM module focus on different interaction-related features and jointly form a better feature representation. Fig. 13 shows the output features of the CFT module, suggesting that the CFT can efficiently transfer affordance knowledge to egocentric view. Fig. 10 shows the co-relation matrix of our

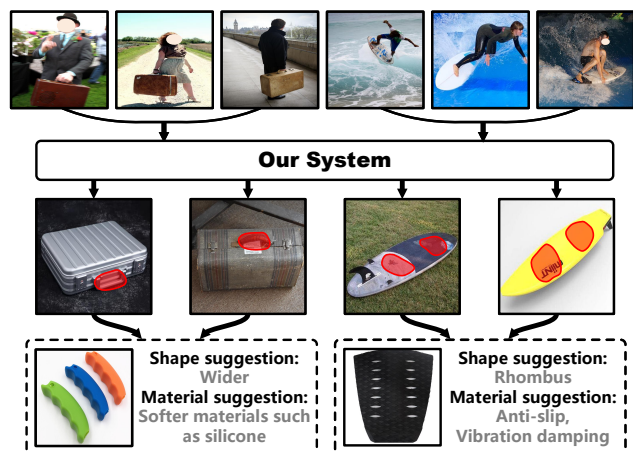


Fig. 17. **Potential Applications: Industrial Manufacturing.** Our system provides the ability to help design the product’s shape and material according to the interaction habits during the manufacturing process.

approach and the model without ACP in the testing phase. It proves that the ACP strategy can help capture the multiple affordance categories to which objects belong, enhancing the network’s capability to perceive affordance regions.

Fig. 14 (a) shows the influence of  $T$  in the ACP strategy on the model.  $T$  has a smoothing effect on the category correlation distribution and plays a preservation role for affordance co-relation. The performance is more sensitive to changes in  $T$  and has a greater impact at larger values. Fig. 14 (b) and (c) show the effect of the channel dimension  $c$  of the features and the rank  $r$  of the dictionary matrix  $W$  in the AIM module, respectively. The value of  $c$  has no significant impact on the results, and the model achieves a slightly better performance at  $c = 512$ . A larger number of channels may increase the complexity of the optimization and lead to a decrease in model performance. Different ranks represent the number of bases of the interaction subfeatures. The best results are obtained when  $r = 64$ . A smaller  $r$  may lead to poor results due to the number of bases being too small to represent the interactions’ sub-features fully. Moreover, a larger  $r$  leads to worse results possibly due to the redundancy of information caused by redundant bases. Fig. 14 (d) shows the impact of the number of exocentric images on model performance, which has a relatively positive effect on model performance as  $N$  increases from 1 to 3. It indicates that the AIM module can capture affordance-specific cues

from multiple images, playing a critical role in affordance region prediction.

## 6 CONCLUSION AND DISCUSSION

In this paper, we make the first attempt to address a challenging task named affordance grounding from exocentric view. Specifically, we propose a novel cross-view affordance knowledge transfer framework that can extract invariant affordance from diverse exocentric interactions and transfer it to egocentric view. We establish a large affordance grounding dataset named AGD20K, which contains 20K well-annotated images, serving as a pioneer testbed for the task. Besides, we expand the scale of the test set from a wide range of different attributes, making the test set more challenging and more suitable for real-world application scenarios. Our model outperforms representative models from related areas and can serve as a strong baseline for future research.

**Future Directions.** Future research could focus on more precisely localizing human body parts (such as the hands, feet, mouth, *etc.*) to interact with objects and recognizing each local region that the human body interacts with based on an exocentric view. Additionally, object affordance area localization could be studied in multimodal scenarios which contain language or audio data.

**Weakness.** Fig. 15 shows some failure cases. Our model may activate irrelevant background when the structure is lengthy and thin, complex, or when the background and foreground cannot be distinguished clearly. Future work could focus on enhancing the associated affordance class regions during training, ignoring the irrelevant background regions [69], and adjusting the obtained results according to affordance properties to produce more accurate predictions [67].

**Potential Applications.** 1) **Learning from demonstrations:** As shown in Fig. 16, our system empowers the agent to efficiently acquire affordance-related knowledge from the human-object interaction in the exocentric view and to locate it in the egocentric image, which enables the agent to operate in the first-person view [16, 3]. 2) **Industrial Manufacturing:** As shown in Fig. 17, our system can explore the object's interaction regions from multiple exocentric views of the human-object interaction and design more suitable shapes and materials to improve product quality during the manufacturing process [74].

## REFERENCES

- [1] J. J. Gibson, "The theory of affordances," *Hilldale*, 1977.
- [2] J. Bohg, K. Hausman, B. Sankaran, O. Brock, D. Kragic, S. Schaal, and G. S. Sukhatme, "Interactive perception: Leveraging action in perception and perception in action," *IEEE Transactions on Robotics*, vol. 33, no. 6, pp. 1273–1291, 2017.
- [3] T. Nagarajan, C. Feichtenhofer, and K. Grauman, "Grounded human-object interaction hotspots from video," in *Proceedings of the IEEE/CVF International Conference on Computer Vision*, 2019, pp. 8688–8697.
- [4] T. Nagarajan and K. Grauman, "Learning affordance landscapes for interaction exploration in 3d environments," *Advances in Neural Information Processing Systems*, vol. 33, pp. 2005–2015, 2020.
- [5] P. Mandikal and K. Grauman, "Learning dexterous grasping with object-centric visual affordances," in *2021 IEEE International Conference on Robotics and Automation (ICRA)*. IEEE, 2021, pp. 6169–6176.
- [6] M. Hassanin, S. Khan, and M. Tahtali, "Visual affordance and function understanding: A survey," *ACM Computing Surveys (CSUR)*, vol. 54, no. 3, pp. 1–35, 2021.
- [7] H. Grabner, J. Gall, and L. Van Gool, "What makes a chair a chair?" in *Proceedings of the IEEE Conference on Computer Vision and Pattern Recognition (CVPR)*. IEEE, 2011, pp. 1529–1536.
- [8] H. S. Koppula, R. Gupta, and A. Saxena, "Learning human activities and object affordances from rgb-d videos," *The International journal of robotics research*, vol. 32, no. 8, pp. 951–970, 2013.
- [9] H. Luo, W. Zhai, J. Zhang, Y. Cao, and D. Tao, "Learning visual affordance grounding from demonstration videos," *arXiv preprint arXiv:2108.05675*, 2021.
- [10] Y. Yang, Z. Ni, M. Gao, J. Zhang, and D. Tao, "Collaborative pushing and grasping of tightly stacked objects via deep reinforcement learning," *IEEE/CAA Journal of Automatica Sinica*, vol. 9, no. 1, pp. 135–145, 2021.
- [11] H. Luo, W. Zhai, J. Zhang, Y. Cao, and D. Tao, "One-shot affordance detection," *arXiv preprint arXiv:2106.14747*, 2021.
- [12] D. D. Lee and H. S. Seung, "Algorithms for non-negative matrix factorization," in *NIPS*, 2000.
- [13] J. Sawatzky, A. Srikantha, and J. Gall, "Weakly supervised affordance detection," in *Proceedings of the IEEE Conference on Computer Vision and Pattern Recognition (CVPR)*, July 2017.
- [14] A. Nguyen, D. Kanoulas, D. G. Caldwell, and N. G. Tsagarakis, "Object-based affordances detection with convolutional neural networks and dense conditional random fields," in *2017 IEEE/RSJ International Conference on Intelligent Robots and Systems (IROS)*. IEEE, 2017, pp. 5908–5915.
- [15] A. Myers, C. L. Teo, C. Fermüller, and Y. Aloimonos, "Affordance detection of tool parts from geometric features," in *2015 IEEE International Conference on Robotics and Automation (ICRA)*. IEEE, 2015, pp. 1374–1381.
- [16] K. Fang, T.-L. Wu, D. Yang, S. Savarese, and J. J. Lim, "Demo2vec: Reasoning object affordances from online videos," in *Proceedings of the IEEE Conference on Computer Vision and Pattern Recognition*, 2018, pp. 2139–2147.
- [17] H. Luo, W. Zhai, J. Zhang, Y. Cao, and D. Tao, "Learning affordance grounding from exocentric images," *arXiv preprint arXiv:2203.09905*, 2022.
- [18] M. Hassanin, S. Khan, and M. Tahtali, "Visual affordance and function understanding: A survey," *arXiv*, 2018.
- [19] T.-T. Do, A. Nguyen, and I. Reid, "Affordancenet: An end-to-end deep learning approach for object affordance detection," in *2018 IEEE international conference on robotics and automation (ICRA)*. IEEE, 2018, pp. 5882–5889.
- [20] C.-Y. Chuang, J. Li, A. Torralba, and S. Fidler, "Learning to act properly: Predicting and explaining affordances from images," in *Proceedings of the IEEE Conference on Computer Vision and Pattern Recognition*, 2018, pp. 975–983.
- [21] X. Zhao, Y. Cao, and Y. Kang, "Object affordance detection with relationship-aware network," *Neural Computing and Applications*, vol. 32, no. 18, pp. 14 321–14 333, 2020.
- [22] H. S. Koppula and A. Saxena, "Physically grounded spatio-temporal object affordances," in *European Conference on Computer Vision*. Springer, 2014, pp. 831–847.
- [23] J. Sawatzky, A. Srikantha, and J. Gall, "Weakly supervised affordance detection," in *Proceedings of the IEEE Conference on Computer Vision and Pattern Recognition*, 2017, pp. 2795–2804.
- [24] J. Sawatzky and J. Gall, "Adaptive binarization for weakly supervised affordance segmentation," in *Proceedings of the IEEE International Conference on Computer Vision Workshops*, 2017, pp. 1383–1391.
- [25] S. Deng, X. Xu, C. Wu, K. Chen, and K. Jia, "3d affordancenet: A benchmark for visual object affordance understanding," in *Proceedings of the IEEE/CVF Conference on Computer Vision and Pattern Recognition*, 2021, pp. 1778–1787.
- [26] W. Zhai, H. Luo, J. Zhang, Y. Cao, and D. Tao, "One-shot object affordance detection in the wild," *IJCV*, 2022.
- [27] J. Mi, S. Tang, Z. Deng, M. Goerner, and J. Zhang, "Object affordance based multimodal fusion for natural human-robot interaction," *Cognitive Systems Research*, vol. 54, pp. 128–137, 2019.
- [28] J. Mi, H. Liang, N. Katsakis, S. Tang, Q. Li, C. Zhang, and J. Zhang, "Intention-related natural language grounding via object affordance detection and intention semantic extraction," *Frontiers in Neurobotics*, p. 26, 2020.

- [29] L. Lu, W. Zhai, H. Luo, Y. Kang, and Y. Cao, "Phrase-based affordance detection via cyclic bilateral interaction," *arXiv preprint arXiv:2202.12076*, 2022.
- [30] A. Roy and S. Todorovic, "A multi-scale cnn for affordance segmentation in rgb images," in *Proceedings of the European Conference on Computer Vision (ECCV)*. Springer, 2016, pp. 186–201.
- [31] M. Stark, P. Lies, M. Zillich, J. Wyatt, and B. Schiele, "Functional object class detection based on learned affordance cues," in *International conference on computer vision systems*. Springer, 2008, pp. 435–444.
- [32] V. Ferrari, T. Tuytelaars, and L. V. Gool, "Object detection by contour segment networks," in *European conference on computer vision*. Springer, 2006, pp. 14–28.
- [33] H. Kjellström, J. Romero, and D. Kragić, "Visual object-action recognition: Inferring object affordances from human demonstration," *Computer Vision and Image Understanding*, vol. 115, no. 1, pp. 81–90, 2011.
- [34] Y. LeCun, F. J. Huang, and L. Bottou, "Learning methods for generic object recognition with invariance to pose and lighting," in *Proceedings of the 2004 IEEE Computer Society Conference on Computer Vision and Pattern Recognition, 2004. CVPR 2004.*, vol. 2. IEEE, 2004, pp. II–104.
- [35] D. F. Fouhey, X. Wang, and A. Gupta, "In defense of the direct perception of affordances," *arXiv preprint arXiv:1505.01085*, 2015.
- [36] N. Silberman, D. Hoiem, P. Kohli, and R. Fergus, "Indoor segmentation and support inference from rgb-d images," in *European conference on computer vision*. Springer, 2012, pp. 746–760.
- [37] V. Hedau, D. Hoiem, and D. Forsyth, "Recovering the spatial layout of cluttered rooms," in *2009 IEEE 12th international conference on computer vision*. IEEE, 2009, pp. 1849–1856.
- [38] A. Nguyen, D. Kanoulas, D. G. Caldwell, and N. G. Tsagarakis, "Detecting object affordances with convolutional neural networks," in *2016 IEEE/RSJ International Conference on Intelligent Robots and Systems (IROS)*. IEEE, 2016, pp. 2765–2770.
- [39] S. R. Lakani, A. J. Rodríguez-Sánchez, and J. Piater, "Can affordances guide object decomposition into semantically meaningful parts?" in *2017 IEEE Winter Conference on Applications of Computer Vision (WACV)*. IEEE, 2017, pp. 82–90.
- [40] A. Srikantha and J. Gall, "Weakly supervised learning of affordances," *arXiv preprint arXiv:1605.02964*, 2016.
- [41] D. Damen, H. Doughty, G. M. Farinella, S. Fidler, A. Furnari, E. Kazakos, D. Moltisanti, J. Munro, T. Perrett, W. Price, and M. Wray, "Scaling egocentric vision: The epic-kitchens dataset," in *European Conference on Computer Vision (ECCV)*, 2018.
- [42] B. Zhou, A. Khosla, A. Lapedriza, A. Oliva, and A. Torralba, "Learning deep features for discriminative localization," in *Proceedings of the IEEE Conference on Computer Vision and Pattern Recognition (CVPR)*, 2016, pp. 2921–2929.
- [43] G. Rizzolatti and L. Craighero, "The mirror-neuron system," *Annu. Rev. Neurosci.*, vol. 27, pp. 169–192, 2004.
- [44] G. A. Sigurdsson, A. Gupta, C. Schmid, A. Farhadi, and K. Alahari, "Actor and observer: Joint modeling of first and third-person videos," in *Proceedings of the IEEE Conference on Computer Vision and Pattern Recognition (CVPR)*, 2018, pp. 7396–7404.
- [45] B. Soran, A. Farhadi, and L. Shapiro, "Action recognition in the presence of one egocentric and multiple static cameras," in *Asian Conference on Computer Vision*. Springer, 2014, pp. 178–193.
- [46] H.-I. Ho, W.-C. Chiu, and Y.-C. F. Wang, "Summarizing first-person videos from third persons' points of view," in *Proceedings of the European Conference on Computer Vision (ECCV)*, 2018, pp. 70–85.
- [47] K. Regmi and M. Shah, "Bridging the domain gap for ground-to-aerial image matching," in *Proceedings of the IEEE International Conference on Computer Vision (ICCV)*, 2019, pp. 470–479.
- [48] C. Fan, J. Lee, M. Xu, K. K. Singh, and J. L. Yong, "Identifying first-person camera wearers in third-person videos," in *2017 IEEE Conference on Computer Vision and Pattern Recognition (CVPR)*, 2017.
- [49] J. Lu, Z. Zhou, X. Zhu, H. Xu, and L. Zhang, "Learning ego 3d representation as ray tracing," *arXiv preprint arXiv:2206.04042*, 2022.
- [50] Y. Li, T. Nagarajan, B. Xiong, and K. Grauman, "Ego-exo: Transferring visual representations from third-person to first-person videos," in *Proceedings of the IEEE Conference on Computer Vision and Pattern Recognition (CVPR)*, 2021, pp. 6943–6953.
- [51] K. He, X. Zhang, S. Ren, and J. Sun, "Deep residual learning for image recognition," in *Proceedings of the IEEE Conference on Computer Vision and Pattern Recognition (CVPR)*, 2016, pp. 770–778.
- [52] T. G. Kolda and B. W. Bader, "Tensor decompositions and applications," *SIAM review*, vol. 51, no. 3, pp. 455–500, 2009.
- [53] Z. Geng, M.-H. Guo, H. Chen, X. Li, K. Wei, and Z. Lin, "Is attention better than matrix decomposition?" *arXiv preprint arXiv:2109.04553*, 2021.
- [54] G. Hinton, O. Vinyals, and J. Dean, "Distilling the knowledge in a neural network," *arXiv preprint arXiv:1503.02531*, 2015.
- [55] T.-Y. Lin, M. Maire, S. Belongie, J. Hays, P. Perona, D. Ramanan, P. Dollár, and C. L. Zitnick, "Microsoft coco: Common objects in context," in *Proceedings of the European Conference on Computer Vision (ECCV)*. Springer, 2014, pp. 740–755.
- [56] Y.-W. Chao, Y. Liu, X. Liu, H. Zeng, and J. Deng, "Learning to detect human-object interactions," in *2018 IEEE winter conference on applications of computer vision (WACV)*. IEEE, 2018, pp. 381–389.
- [57] K. Soomro, A. R. Zamir, and M. Shah, "Ucf101: A dataset of 101 human actions classes from videos in the wild," *arXiv preprint arXiv:1212.0402*, 2012.
- [58] Y. Lv, J. Zhang, Y. Dai, A. Li, N. Barnes, and D.-P. Fan, "Towards deeper understanding of camouflaged object detection," *arXiv preprint arXiv:2205.11333*, 2022.
- [59] Y. Li, X. Hou, C. Koch, J. M. Rehg, and A. L. Yuille, "The secrets of salient object segmentation," in *Proceedings of the IEEE conference on computer vision and pattern recognition*, 2014, pp. 280–287.
- [60] Z. Bylinskii, T. Judd, A. Borji, L. Itti, F. Durand, A. Oliva, and A. Torralba, "Mit saliency benchmark," 2015.
- [61] Z. Bylinskii, T. Judd, A. Oliva, A. Torralba, and F. Durand, "What do different evaluation metrics tell us about saliency models?" *IEEE transactions on pattern analysis and machine intelligence*, vol. 41, no. 3, pp. 740–757, 2018.
- [62] T. Judd, F. Durand, and A. Torralba, "A benchmark of computational models of saliency to predict human fixations," 2012.
- [63] M. J. Swain and D. H. Ballard, "Color indexing," *International Journal of Computer Vision (IJCV)*, vol. 7, no. 1, pp. 11–32, 1991.
- [64] M. Cornia, L. Baraldi, G. Serra, and R. Cucchiara, "A deep multi-level network for saliency prediction," in *2016 23rd International Conference on Pattern Recognition (ICPR)*. IEEE, 2016, pp. 3488–3493.
- [65] M. Kümmerer, T. S. Wallis, and M. Bethge, "Deepgaze ii: Reading fixations from deep features trained on object recognition," *arXiv preprint arXiv:1610.01563*, 2016.
- [66] J. Mai, M. Yang, and W. Luo, "Erasing integrated learning: A simple yet effective approach for weakly supervised object localization," in *Proceedings of the IEEE Conference on Computer Vision and Pattern Recognition (CVPR)*, 2020, pp. 8766–8775.
- [67] X. Pan, Y. Gao, Z. Lin, F. Tang, W. Dong, H. Yuan, F. Huang, and C. Xu, "Unveiling the potential of structure preserving for weakly supervised object localization," in *Proceedings of the IEEE Conference on Computer Vision and Pattern Recognition (CVPR)*, 2021, pp. 11 642–11 651.
- [68] W. Gao, F. Wan, X. Pan, Z. Peng, Q. Tian, Z. Han, B. Zhou, and Q. Ye, "Ts-cam: Token semantic coupled attention map for weakly supervised object localization," in *Proceedings of the IEEE International Conference on Computer Vision (ICCV)*, October 2021, pp. 2886–2895.
- [69] P. Wu, W. Zhai, and Y. Cao, "Background activation suppression for weakly supervised object localization," in *Proceedings of the IEEE Conference on Computer Vision and Pattern Recognition (CVPR)*, 2021.
- [70] Y. Huang, M. Cai, Z. Li, and Y. Sato, "Predicting gaze in egocentric video by learning task-dependent attention transition," in *Proceedings of the European Conference on Computer Vision (ECCV)*, 2018, pp. 754–769.
- [71] S. Liu, S. Tripathi, S. Majumdar, and X. Wang, "Joint hand motion and interaction hotspots prediction from egocentric videos," *arXiv preprint arXiv:2204.01696*, 2022.
- [72] R. J. Peters, A. Iyer, L. Itti, and C. Koch, "Components of bottom-up gaze allocation in natural images," *Vision research*, vol. 45, no. 18, pp. 2397–2416, 2005.
- [73] K. Simonyan and A. Zisserman, "Very deep convolutional networks for large-scale image recognition," *arXiv preprint arXiv:1409.1556*, 2014.
- [74] M. Lau, K. Dev, W. Shi, J. Dorsey, and H. Rushmeier, "Tactile mesh saliency," *ACM Transactions on Graphics (TOG)*, vol. 35, no. 4, pp. 1–11, 2016.